Fast-marching segmentation of three-dimensional intravascular ultrasound images: A pre- and post-intervention study

Marie-Hélène Roy Cardinal[a]
Laboratory of Biorheology and Medical Ultrasonics (LBUM), University of Montreal Hospital Research Center (CRCHUM), Montreal, Quebec H2L 2W5, Canada and Institute of Biomedical Engineering, University of Montreal, Montreal, Quebec H3T 1J4, Canada

Gilles Soulez
Department of Radiology, University of Montreal Hospital, Montreal, Quebec H2L 4M1, Canada and Department of Radiology, Radio-Oncology and Nuclear Medicine, University of Montreal, Montreal, Quebec H3T 1J4, Canada

Jean-Claude Tardif
Montreal Heart Institute, Montreal, Quebec H1T 1C8, Canada and Department of Medicine, University of Montreal, Montreal, Quebec H3T 1J4, Canada

Jean Meunier
Department of Computer Science and Operations Research, University of Montreal, Montreal, Quebec H3T 1J4, Canada and Institute of Biomedical Engineering, University of Montreal, Montreal, Quebec H3T 1J4, Canada

Guy Cloutier[b]
Laboratory of Biorheology and Medical Ultrasonics (LBUM), University of Montreal Hospital Research Center (CRCHUM), Montreal, Quebec H2L 2W5, Canada; Institute of Biomedical Engineering, University of Montreal, Montreal, Quebec 3HT 1J4, Canada; and Department of Radiology, Radio-Oncology and Nuclear Medicine, University of Montreal, Montreal, Quebec H3T 1J4, Canada

Purpose: Intravascular ultrasound (IVUS) is a vascular imaging technique that is used to study atherosclerosis since it has the ability to show the lumen and the vessel wall. Cross-sectional images of blood vessels are produced and they provide quantitative assessment of the vascular wall, information about the nature of atherosclerotic lesions, as well as the plaque shape and size. Due to the ultrasound speckle, catheter artifacts, or calcification shadows, the automated analysis of large IVUS data sets represents an important challenge.
Methods: A multiple interface 3D fast-marching method is presented for the detection of the lumen and external vessel wall boundaries. The segmentation is based on a combination of region and contour information, namely, the gray level probability density functions of the vessel structures and the intensity gradient. The detection of the lumen boundary is fully automatic. The segmentation method includes an interactive initialization procedure of the external vessel wall border. The segmentation method was applied to 20 *in vivo* IVUS data sets acquired from femoral arteries. This database contained three subgroups: Pullbacks acquired before balloon angioplasty ($n=7$), after the intervention ($n=7$), and at a 1 yr follow-up examination ($n=6$). Results were compared to validation contours that were manually traced by two experts on more than 1500 individual frames.
Results: For all subgroups, no significant difference was found between the area measurements of the segmentation and validation contours for the lumen and external vessel wall. Moreover, high intraclass correlation coefficients (>0.96) between the area of the manually traced contours and detected boundaries with the fast-marching method were obtained for both vessel layers over the whole database. The segmentation performance was also evaluated with point-to-point contour distances between segmentation results and manually traced contours. A good overall accuracy was obtained with average distances <0.13 mm and maximum distances <0.46 mm, indicating a good performance in regions lacking information or containing artifacts. Only small differences of less than a pixel (0.02 mm) were observed between the average distance metrics of each subgroup, which prove the segmentation consistency.
Conclusions: This new IVUS segmentation method provides accurate results that correspond well to the experts' manually traced contours, but requires much less manual interactions and is faster. © *2010 American Association of Physicists in Medicine.* [DOI: 10.1118/1.3438476]

I. INTRODUCTION

Intravascular ultrasound imaging (IVUS) provides high-resolution tomographic images of the lumen and vessel wall as a transducer mounted on a catheter is pulled back inside blood vessels. IVUS can be safely used to assess the atherosclerotic plaque progression/regression in clinical trials[1] and it has also been the case in several studies that evaluated the effect of therapies on coronary atherosclerosis.[2,3] Benefits of IVUS-based studies include smaller patient numbers to confirm study end-points and shorter trial durations.[4] With its ability to show the lumen cross section area, the wall thickness, and the volume and position (concentricity or eccentricity) of the lesion, IVUS is also becoming a tool of choice in the treatment of peripheral diseases.[5] Better stent expansion evaluation[6] and understanding of in-stent restenosis mechanisms[7] resulted from IVUS studies. More recently, several reports that investigated, based on IVUS imaging, drug-eluting stent deployment, implantation, and failures were reviewed.[8]

A typical IVUS pullback contains hundreds of images in which the lumen and external elastic membrane [(EEM) the outer layer of the vessel wall] must be identified. Several 2D and 3D quantitative measurements of the atherosclerotic disease such as the plaque volume, wall thickness, vascular remodeling, lumen area stenosis, and plaque burden can be made from these contours.[9] Since clinical trials often require numerous patients (>100) to investigate atherosclerosis therapies, a tremendous amount of data are produced and the analysis is fastidious without robust and easy to use image processing methods. Moreover, IVUS imaging is subject to catheter ring-down artifacts, missing vessel parts due to calcification shadowing or side branches, pulsation movements, heterogeneously looking plaque, and ultrasonic speckle. Specific segmentation models must then be elaborated to overcome these difficulties.

Many segmentation methods have been proposed so far for the assessment of coronary IVUS images. The vast majority of these algorithms were based on edge information. Recent works include graph-search algorithms with implementations based on the information of edge operators applied to blood noise filtered images,[10] and on first-derivative and second-derivative gradient filters.[11] Active contours and surfaces were investigated with various edge information: Gradient-based active surfaces,[12] pixel intensity combined to gradient active contours,[13] gradient vector flow active contours based on edge information with median filtered images,[14] and image gray level gradient active contours with automatic initialization.[15] Other edge-based segmentation models include elliptical template fitting[16] and multiagent segmentation.[17] On the other hand, segmentation models were developed using region features of IVUS images: The optimization of a maximum *a posteriori* estimator modeling gray level variances and contour geometry was proposed[18] and then revised using Rayleigh statistics of the signal for the detection of the lumen contour only.[19] A graph-search algorithm also using Rayleigh statistics and intensity patterns learned from a training step were also proposed.[20] None of these segmentation methods combines local edge information and region features.

Furthermore, these investigations were all focused on the analysis of coronary IVUS images that are widely studied. Because the usage of IVUS is becoming a valued and sometimes necessary tool in peripheral artery interventions, and as the appearance and size of peripheral arteries are different,[5] the IVUS segmentation problematic should also be addressed for these vessels. In cases where the disease is advanced and intervention is required, extensive irregular atheromas that project into the lumen are routinely found in peripheral vessels.[21] Since IVUS is a gold standard method for clinical trials, the segmentation algorithm should be validated with IVUS acquisitions ideally acquired at different time points during such a trial (for example, before and after balloon angioplasty and one year after pharmaceutical or other therapies). Previously, we presented a 3D fast-marching segmentation model that was based on the gray level probability density functions (PDFs) of the vessel wall structures.[22] However, the segmentation method was initialized manually. Segmentation results compared well to a gradient implementation of the fast-marching method.

The aim of this work was thus to identify the luminal and EEM borders on IVUS sequences of diseased femoral arteries with a highly automated segmentation method. A fast-marching segmentation model with an automated initialization procedure that requires minimal user involvement is thus presented. This method has the ability to recover in parallel different boundaries. During the initialization, the lumen and EEM contours are automatically detected and the EEM contours, on longitudinal views of the 3D data set, can be corrected manually if required. The automatically estimated PDFs that model the gray level distributions of the wall layers and atherosclerotic plaques are shown to be appropriate for the segmentation of the femoral arterial wall that exhibits various sizes and echogenicities. The image gradient information was combined with PDF mixtures representing the vessel wall structures to give more robustness to the multiple interface fast-marching segmentation. Overall, 20 pullbacks containing 15 895 frames were segmented and more than 1500 frames were analyzed manually for accuracy assessment of our method. Such a comparison with pre- and post-intervention data has never been reported in the IVUS segmentation literature (for both coronary and peripheral vessels).

The paper is organized as follows: The 3D fast-marching method based on a mixture of probability density functions and the gray level gradient is detailed in Sec. II; it is followed by the description of the PDF estimation method and the initialization procedure. Section III presents the experimental data. Segmentation results are reported in Sec. IV and discussed in Sec. V.

II. SEGMENTATION MODEL

The segmentation model is divided into three steps: The preprocessing, the initialization, and the fast-marching segmentation. Figure 1 shows a block diagram of the whole segmentation process.
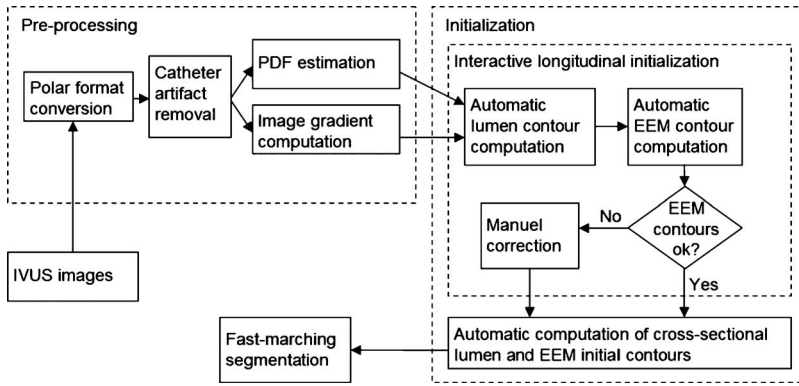
II.A. Fast-marching method

Level-set and fast-marching methods, which were introduced by Osher and Sethian to follow an interface (or front or contour) propagating under a speed function F,[23,24] have been widely used in the medical imaging field ever since they were adapted to shape recovery.[25] When applied to image segmentation, the boundary is defined as the desired final position of the propagating interface. To achieve this, the interface speed should become close to zero when it reaches the object borders to stop the propagation and end the segmentation process.

When using the fast-marching formulation for the segmentation of a 3D image sequence, the function T that describes the arrival time $T(x)$ of the propagating contour at a point $x=(x_1,x_2,x_3)$ in the imaging volume governs the front evolution. The T function satisfies Eq. (1), stating that the arrival time difference between two adjacent voxels increases as the velocity of the contour F decreases. The evolution of the interface is performed through the construction of the time function map (T map)[23]

$$|\nabla T|F = 1. \tag{1}$$

For the segmentation of IVUS images, the luminal and EEM borders must be identified. In our study, both contours were detected in parallel using a multiple interface extension of the fast-marching algorithm.[26] The multiple interface approach directly depicts the layered structure of the wall and prevents the detected borders from overlapping. For this particular case, a boundary is defined by the meeting position of two fronts propagating in opposite directions. The final position of the boundary is thus located where the speed is minimal for both opposite interfaces. To identify the lumen and EEM borders, two sets of two interfaces propagating until they meet were defined. Each of the multiple interfaces $l \in L$, where L is the set $\{1,2,\ldots,2N_L\}$ of interfaces of the $N_L=2$ vessel wall structures, propagates according to a speed function defined in terms of the image gradient and the PDF P_l of the corresponding wall component. For example, to detect the lumen boundary, the first interface, positioned inside the lumen, evolves outward according to the lumen PDF and the intensity gradient; the second interface, positioned inside the intima plus plaque structure of the wall, evolves inward according to the intima plus plaque PDF and the

intensity gradient (the EEM border is similarly detected with two moving interfaces). The propagation speed F_l of interface l is given by Eq. (2)

$$F_l(i,j,k) = \alpha F_{l,\mathrm{PDF}}(i,j,k) + \beta F_{l,\mathrm{grad}}(i,j,k), \tag{2}$$

where $F_{l,\mathrm{PDF}}(i,j,k)$ and $F_{l,\mathrm{grad}}(i,j,k)$ are the speed function components, at position (i,j,k) in the IVUS image volume I, respectively defined in terms of the PDF and intensity gradient; α and β are the weights of each component in the speed function F_l that should be in the interval $[0, 1]$.[26] $F_{l,\mathrm{PDF}}(i,j,k)$ and $F_{l,\mathrm{grad}}(i,j,k)$ were defined in this study as

$$F_{l,\mathrm{PDF}}(i,j,k) = \frac{1}{N_\nu}\sum_{s\in\nu} p_l(y_s), \tag{3}$$

$$F_{l,\mathrm{grad}}(i,j,k) = \frac{1}{1+|G_\sigma * g(y_s)|}, \tag{4}$$

where y_s is the gray level value of voxel s positioned at $I(i,j,k)$; ν is the set of the N_ν 3D neighbors of the voxel s; and $p_l(y_s)$ is the occurring probability of y_s in region l. According to Eq. (3), the velocity of interface l takes higher values when it is inside a region having a gray level distribution close to p_l, whereas the velocity decreases when approaching the boundary since the neighbors are distributed under other component PDFs. This velocity function has a general form that can be used with any type of PDF. In Eq. (4), $g(y_s)$ is the value of the gradient g at y_s and G_σ is a Gaussian smoothing filter of standard deviation $\sigma=3.5$ pixels (the dimension of the IVUS images was 10×10 mm^2 with an isotropic pixel size of 0.026×0.026 mm^2; the vessel diameter of the superficial femoral arteries were 6.0 mm, on average, in this study). According to Eq. (4), the speed function takes low values when the gradient is high, which corresponds to the border between different regions.

The propagation of multiple interfaces is similar to the single interface fast-marching algorithm except that several interfaces contribute to the construction of a joint T map (Sifakis *et al.*[26] provided a detailed description of the T map construction algorithm). The multiple interface fast-marching segmentation is finished when all fronts propagating in op-
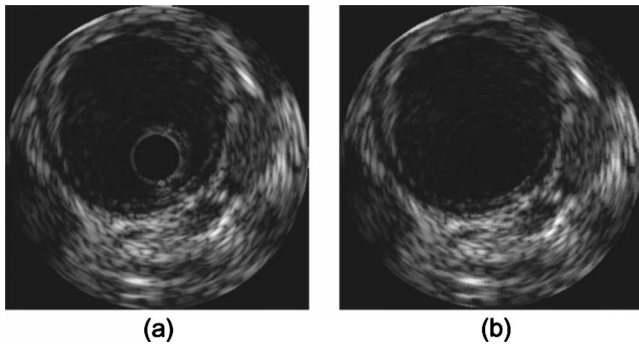
FIG. 2. (a) Typical intravascular ultrasound cross-sectional image with ring-down artifact and (b) corresponding image without the artifact.

posite directions have met. Fronts are thus obligated to evolve until the arrival time map is completely built.

II.B. Preprocessing

The IVUS images were converted to the polar format to enable the usage of a radial window in Eq. (3) and the computation of a radial gradient in Eq. (4). All computations were performed in the polar format. The radial 3D window that provided neighborhood averaging in the PDF component of the speed function was of size $3°$ radially $\times 0.3$ mm axially $\times 0.3$ mm longitudinally (3 $\times 12 \times 3$ voxels, $N_v = 108$). The α and β parameters in Eq. (2) were set to 0.5. For the gradient computation, each radial line of the smoothed polar transformed image was convolved with the gradient operator $[2\ 2\ 1\ 0{-}1{-}2{-}2]$. The gradient at each point was then averaged with both axial neighbors and normalized between $[-1, 1]$.

The catheter artifact (ring-down) was also automatically detected and removed from the IVUS images. Pixels that had intensities that correlated highly (with $r > 0.9$) through frames across the whole pullback were labeled as catheter pixels. Since the blood pixels decorrelate as well as the wall pixels over the whole pullback, it was possible to distinguish the catheter from the blood and wall. The search length for each scan line was reduced to the first 30% points (corresponding to a circular area with a 1.5 mm radius) and the correlation was performed on a subset of the whole pullback (corresponding to 5% of the number of images) to reduce the computation. The size of the searched region, determined empirically, was wide enough to cover large ring-down artifacts. The labeled catheter pixel intensities were replaced by the average intensity of the eight connected noncatheter pixel neighbors to preserve the plaque in the image if the artifact and parts of the vessel wall were superimposed. Figure 2 shows an example of an IVUS image before and after the catheter artifact removal procedure.

II.C. Probability density function estimation

The speed function of Eq. (3) is based on the occurring probability of the gray level values $[p_l(y_s)]$ in the different vessel components. It is usually assumed in ultrasound B-mode imaging (the B-mode signal is the envelop filtered

radio-frequency signal) that the intensity of the ultrasonic speckle pattern of a tissue that contains a large number of randomly distributed scatterers is Rayleigh distributed.[27] The gray level distributions of the tissue components in the IVUS volume were thus each modeled with a Rayleigh PDF. Since an IVUS pullback contains the ultrasonic speckle pattern of various tissues (blood in the lumen, plaque components, vessel wall, and different types of surrounding tissues), its distribution was modeled as a mixture of Rayleigh PDFs. The PDF mixture $p_{Y|\Theta}$ with parameter $\Theta = \{(\omega_m, a_m^2)\}_{m=1}^M$ that contains M Rayleigh probability density functions $p_Y(y_s)$ was defined by

$$p_{Y|\Theta}(y_s | \Theta) = \sum_{m=1}^{M} \omega_m p_m(y_s | a_m^2),\qquad(5)$$

with

$$p_Y(y_s; a^2) = \frac{y_s}{a^2} \exp\left(-\frac{y_s^2}{2a^2}\right),\qquad(6)$$

where ω_m is the proportion of the m_{th} component of the mixture so that $\sum_{m=1}^M \omega_m = 1$; Y is the image gray levels and y_s takes its value in $[1, \ldots, 256]$; and $a^2 > 0$ and the variance $\sigma^2 = a^2(4 - \pi)/2$.

The global mixture PDF is thus the combination of the intensity distributions of the different tissues that form the IVUS data. The expectation-maximization (EM) algorithm[28] was used to estimate the mixture parameter Θ from the whole IVUS pullback. A detailed description of the Rayleigh PDF mixture parameter estimation for IVUS pullbacks with the expectation-maximization algorithm can be found in our previous work.[22] With the EM algorithm, the mixture parameters were automatically computed at the beginning of each segmentation to take into account the echogenicity variability among patients. The only fixed parameter was the number of distribution in the mixture. A mixture of $M = 5$ distributions (roughly corresponding to the lumen, plaque components, vessel wall, and two types of surrounding tissues) was used to model each IVUS data set.

For computation efficiency, the EM algorithm was only applied to a subset of Y, i.e., the pixel intensities of the whole IVUS series of a given patient. The subset contained approximately 3% of the pixels that were randomly sampled from the whole pullback frames. It was shown that no statistically significant difference was found between the Rayleigh mixture parameters calculated for such a subset and the whole observed data set.[22]

II.C.1. PDF classification

To be used in the multiple interface fast-marching, the different distributions of the mixture must be assigned to the tissues that form the IVUS data. For the initial interface calculation (see Sec. II D), a first rough assignment was performed. The distributions were thus classified in two groups: The hypoechoic tissue group that contains the lumen and media structure (which appears, on axial frames, as a thick hypoechoic ring inside the EEM) (group 1) and the higher
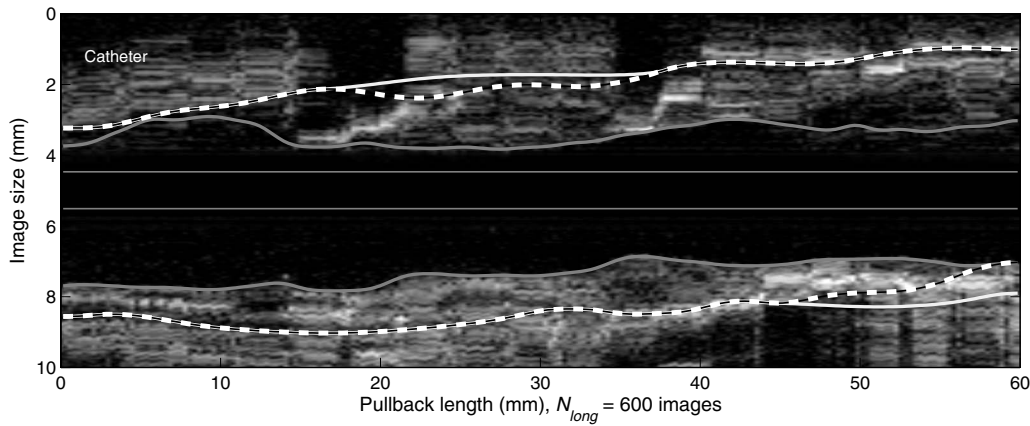
FIG. 3. Example of a LView of an IVUS data set with the longitudinal initialization contours, which required manual corrections of the EEM. The thick gray lines, one on each side of the catheter, correspond to the initial longitudinal lumen contours automatically detected. The white dotted lines are the automatically computed longitudinal EEM contours proposed to the user for manual acceptance or correction. The thick white lines correspond to the manual corrections. The catheter position was outlined with the thin gray lines. N_{long} is the number of IVUS frames in the pullback.

intensity tissue group that represents the intima plus plaque and surrounding tissues (group 2). The two distributions with the lowest average value were assigned to the first group and the remaining three distributions to the second one. This was a rough estimate that was only used during the initialization procedure. For the fast-marching segmentation, the distributions used in Eq. (3) were chosen to minimize the difference between the selected PDF for the lumen or wall components and the gray level histograms computed from the corresponding regions delineated by the initial contours. The speed function $F_{l,\text{PDF}}$ was thus defined according to the PDF that best fitted the tissue echogenicity.

II.D. Interactive initialization

The initialization procedure was divided in two steps. Initial lumen and EEM borders were computed on longitudinal views (LViews) during the first step of the initialization procedure. LViews provide information for the whole pullback. A total of four LViews were thus selected at regularly spaced angles over 360° (0°, 45°, 90°, and 135°); they provided enough information on each cross-sectional image while limiting the computation time. Initial longitudinal lumen contours were fully automatically detected. The EEM longitudinal contours were also automatically computed and then proposed to the user for correction or acceptance on the four LViews.

The fully automatic calculation of the cross-sectional (or axial) lumen and EEM initial borders of the individual frames was performed during the second step of the initialization process. The cross-sectional contours were computed from the initial longitudinal contours. No manual corrections were necessary or used at this step. Details on the initialization steps 1 and 2 are given below.

II.D.1. Longitudinal Initialization

Sets of two longitudinal lumen contours (one on each side of the catheter) were first automatically detected on the four LViews for a total of 8 boundaries. The two thick gray lines

in Fig. 3 are an example of detected initial longitudinal lumen contours on an IVUS LView. Each longitudinal contour c_{Lum}, where Lum indicates the lumen, was grown, starting at the catheter position, to maximize the lumen boundary likelihood L_{Lum}

$$L_{\text{Lum}}(c_{\text{Lum}}) = \frac{1}{N_{\nu 1}} \sum_{s \in \nu 1} \log p_1(y_s), \tag{7}$$

where $\nu 1$ is the set of $N_{\nu 1}$ voxels inside the lumen boundary and outside the catheter and $p_1(y_s)$ is the estimated occurring probabilities of voxel y_s in the hypoechoic tissue group 1. Pixels were added to the set $\nu 1$ as long as the log-likelihood of their neighborhood was higher than 95% of the lumen boundary likelihood L_{Lum}. The neighborhood was defined by a window of 0.08 mm radially, 0.08 mm longitudinally, and 0.08 mm axially ($3 \times 3 \times 3$ voxels). The longitudinal contours were then smoothed as B-splines to remove inconsistent points. This method was simple and fast, and provided initial longitudinal contours that were rough initialization of the lumen to be refined in the last step of the initialization process (see Sec. II D 2).

EEM longitudinal borders were then detected on the same LViews. For that purpose, the low intensity media surrounded by the adventitia that brightly reflects the ultrasound waves was searched in the IVUS LViews. The vessel contours c_{EEM} contained the previously identified longitudinal lumen and were positioned to maximize the EEM boundary likelihood defined by

$$L_{\text{EEM}}(c_{\text{EEM}}) = \frac{1}{N_{\nu 1}} \sum_{s \in \nu 1} \log p_1(y_s) + \frac{1}{N_{\nu 2}} \sum_{s \in \nu 2} \log p_2(y_s)$$
$$+ \frac{1}{N_{\nu 3}} \sum_{s \in \nu 3} g(y_s), \tag{8}$$

where $\nu 1$ and $\nu 2$ are sets of $N_{\nu 1}$ and $N_{\nu 2}$ voxels in regions of interest, respectively inside and outside the vessel boundary; $\nu 3$ is the set of $N_{\nu 3}$ voxels on the boundary; $p_1(y_s)$ and $p_2(y_s)$ are the estimated occurring probabilities of y_s in the hypo-

echoic and higher intensity tissue regions, respectively; and $g(y_s)$ is the value of the gray level gradient g at y_s. L_{EEM} reached a maximum when the pixels inside and outside the vessel boundary were distributed according to the hypoechoic and hyperechoic tissue distributions, respectively, and when the pixels close to the boundary had a high intensity gradient.

To maximize Eq. (8), deformation transformations were applied to the longitudinal EEM boundary c_{EEM} at regularly spaced control points. A simplified deformable template strategy[29] was used to modify the longitudinal EEM boundary with 1D stretching transformations applied in the radial direction only. The stretching deformations were performed according to Eq. (9) by displacing the contour c_1 with various Gaussian windows w centered on the control point position k_{ctrl}.

$$c_2(k) = c_1(k) + \gamma_w w(k), \tag{9}$$

with

$$w(k) = e^{-(k - k_{ctrl})^2/2\sigma^2},$$

where c_1 is the contour to deform and c_2 the deformed contour; $k=[1,\ldots,N_{long}]$ and $1 \le k_{ctrl} \le N_{long}$; N_{long} is the number of points in the longitudinal contour (equal to the number of IVUS frames in the pullback); γ_w is a scaling factor of the window; k_{ctrl} is the control point position; and σ^2 is the variance of the Gaussian window. Parameters in Eq. (9) were set to -1.2 mm $\le \gamma_w \le 1.2$ mm, $\sigma=40$, and $N_{ctrl}=20$ regularly spaced control points. These values were determined empirically to provide a large enough searching window and to make the contour flexible while keeping a low computation time.

On the first LView at 0°, the deformations were applied to the longitudinal EEM boundary that was initially positioned outside the longitudinal lumen location since no information was available on its position. On the following three LViews, deformations were applied to the previously detected EEM border in a restrained neighborhood of the longitudinal contour to maximize L_{EEM} locally. The detected longitudinal contours were proposed to the user and corrected if necessary before proceeding to the next LView. Corrections were made by dragging the erroneous parts of the contour close to the boundary while keeping the accurately detected parts of the boundary. Figure 3 shows an example of LView that required manual corrections of the EEM contours. The detected and corrected longitudinal EEM contours are displayed.

II.D.2. Automatic cross-sectional initialization

From the previous longitudinal IVUS initialization procedure, two sets of eight contour points, for the lumen and EEM, were available for the initialization of all cross-sectional frames. Figure 4 shows an example of an IVUS cross-sectional frame in the polar format with the corresponding two sets of eight longitudinal contour points. Axial (along depth) lumen and EEM contours were detected inside a region around these longitudinal contour points to reduce
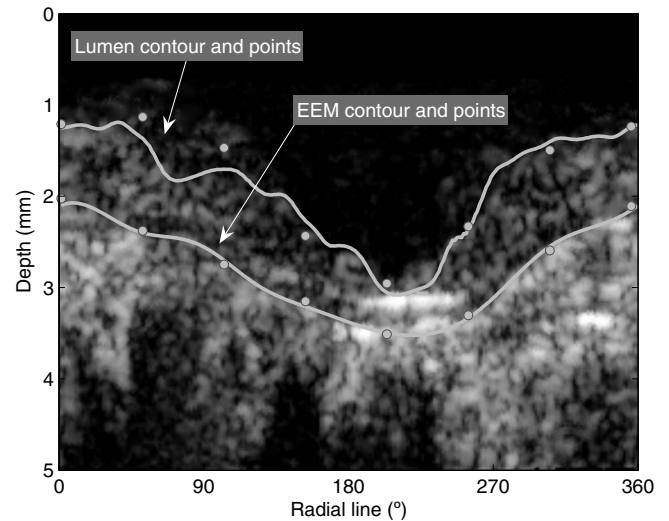

FIG. 4. Example of a cross-sectional IVUS frame in polar format with the initial longitudinal set of eight contour points and automatically computed axial contours for both the lumen and EEM.

the searching area and computation time. A similar procedure to the EEM longitudinal boundary detection based on Eqs. (8) and (9), without the manual interaction, was used to initialize the axial lumen and EEM.

The initial cross-sectional lumen contours were automatically detected as smooth closed curves, not necessarily circular to preserve the irregular lumen shape. A spline interpolated contour passing through the initial longitudinal lumen points was thus deformed to maximize the lumen boundary likelihood defined similarly to the EEM boundary likelihood in Eq. (8). The deformed contour was not restricted to pass through the longitudinal contour points. However, for the lumen initialization, $v1$ in Eq. (8), which is the set of pixels in a region of interest inside the boundary, contained the pixels inside the whole lumen and $v2$ contained the set of pixels outside the lumen boundary (corresponding to the intima plus plaque).

On the other hand, the initial axial propagating interface for the external wall boundary was automatically set as an elliptical contour, passing near the longitudinal EEM contour points and maximizing the vessel boundary likelihood $L_{EEM}(c_{EEM})$ of Eq. (8) for the cross-sectional images.

Once initialized, stretching transformations, as defined in the previous section by Eq. (9), were applied to both lumen and EEM cross-sectional contours to maximize their boundary likelihood. Deformations applied to the axial contours were characterized by parameters $\sigma=\{40,60\}$, -0.25 mm $\le \gamma_w \le 0.25$ mm, and $N_{ctrl}=20$ control points in Eq. (9). These values were also determined empirically; a smaller search window was used here since only small adjustments of the axial contours were performed. Examples of automatically computed cross-sectional contours for the lumen and EEM are shown on Fig. 4.

Cross-sectional lumen and EEM contours were computed for one out of three IVUS images and interpolated for the missing frames to reduce the computation time. The fast-

marching segmentation was initialized with the interpolated contours and was performed over the whole data set. As mentioned earlier, the multiple interface fast-marching segmentation requires that the initial axial contours be converted in pairs of interfaces propagating in opposite directions and that they contain the boundary to be detected. This was performed using the procedure described in our previous work.[22]

III. EXPERIMENTAL DATA

A total of 20 *in vivo* IVUS pullbacks (of 795 ± 308 frames/series for a total of 15 895 frames) from diseased superficial femoral arteries of 11 patients were available. Of these data sets, seven were acquired before undergoing balloon angioplasty, seven were acquired following intervention (balloon angioplasty), and finally, six were obtained at a 1 yr follow-up examination (the database of 20 IVUS pullbacks selected for the validation study was arbitrarily chosen from the data set of 11 patients to provide groups of approximately the same size). The data sets were thus divided into three subgroups. The patients received external beam radiation (doses between 0 and 14 Gy) 24 h after intervention. The IVUS database was acquired as a substudy of a randomized clinical trial.[30]

An IVUS Volcano Therapeutics imaging system (InVision Gold, Rancho Cordova, CA) equipped with a 20 MHz array transducer was used to acquire data. The frame rate was set to 10 images/s and the catheter pullback velocity to 1 mm/s; 0.1 mm thick 2D slices were thus generated. The acquisition was not ECG-gated. Images of size 10×10 mm^2 were recorded as 384×384 pixel matrices and stored in the DICOM format.

III.A. Validation

To validate the segmentation results, comparisons were made with manually drawn contours of the lumen and EEM. Boundaries were traced by two independent experts from an accredited IVUS core laboratory on one every ten frames of each IVUS pullback for a total of 1593 IVUS images available for the validation. Of these frames, 459 came from the preangioplasty group, 476 from the post-intervention group, and 658 from the 1 yr follow-up examination group. The experts did not draw the boundary if its position could not be identified due to excessive noise deterioration or large calcifications. These frames would be rejected in the clinical setting. A total of 1533 and 1524 IVUS frames, respectively, for the lumen and EEM (from the 1593 IVUS frames), were thus manually analyzed. Only approximately 4% of the validation frames were rejected.

Average and Hausdorff point-to-point distances[31] between the detected and manually traced contours were computed to assess the segmentation accuracy. The area of these contours was also computed. The combination of distance and area metrics validates the position and the size of the detected contours compared to the manually traced ones. These metrics were computed for the lumen and EEM borders. The

TABLE I. Segmentation accuracy: Area measurements for the detected boundaries and manually traced contours by the experts. Expert 1 and Expert 2 correspond to the area measurements from the manually traced contours, and FMM 1 and FMM 2 from the detected boundaries with the fast-marching method (both runs). EEM is the external elastic membrane (the vessel wall border). Pre-interv, Post-interv, and Follow-up, respectively, show the results for the pre-intervention (balloon angioplasty), post-intervention, and 1 yr follow-up examination groups. The pixel size is 26×26 μm^2. No significant difference existed when not indicated.

	Expert 1	Expert 2	FMM 1	FMM 2
Lumen area (mm^2)				
All data ($N=1533$)	15.3 ± 5.9 [a–c]	16.0 ± 6.0 [a]	16.1 ± 5.8 [b]	16.2 ± 5.8 [c]
Pre-interv ($N=440$)	15.2 ± 5.5	15.9 ± 5.5	16.3 ± 5.0	16.3 ± 5.0
Post-interv ($N=453$)	15.6 ± 5.0	16.6 ± 5.0	16.6 ± 5.1	16.8 ± 5.3
Follow-up ($N=640$)	15.1 ± 6.8	15.8 ± 6.9	15.7 ± 6.6	15.7 ± 6.6
EEM area (mm^2)				
All data ($N=1524$)	28.5 ± 7.4	28.6 ± 7.4	28.5 ± 7.3	28.5 ± 7.3
Pre-interv ($N=451$)	28.1 ± 4.7	28.1 ± 4.7	28.2 ± 4.5	28.2 ± 4.6
Post-interv ($N=442$)	29.8 ± 4.8	29.8 ± 4.7	29.8 ± 4.8	29.7 ± 4.8
Follow-up ($N=631$)	27.9 ± 9.7	28.2 ± 10.0	27.9 ± 9.7	27.9 ± 9.8

[a]Indicates statistically significant differences ($p<0.01$) between Expert 1 and Expert 2.
[b]Between Expert 1 and FMM 1 ($p<0.01$).
[c]Between Expert 1 and FMM 2 ($p<0.01$).

Hausdorff distance is the maximum distance between different contours; it represents the largest segmentation error or difference between contours (worst case). To evaluate the interuser variability, the contours manually traced by the two experts were also compared.

Moreover, the repeatability of the segmentation was evaluated; each IVUS pullback was segmented two times (including the mixture parameter detection and interactive initialization). The interactive initialization of the method was performed by a qualified user blinded to the validation experts. Average and Hausdorff point-to-point contour distances, and area differences between detected boundaries from different runs of the algorithm were thus calculated.

III.B. Statistical analysis

Two way analyses of variance (ANOVA) were carried out for the area measurements, and average and Hausdorff distances; multiple *pairwise* comparisons with Tukey tests were performed. The area measurements from the whole data sets and for each subgroup (preangioplasty, postangioplasty, and follow-up examination) were computed. The average and Hausdorff distances were also evaluated for each subgroup (preangioplasty, postangioplasty, and follow-up examination). In the first ANOVA, the comparison was made between the area measurements of the segmentation and the experts' contours (see Table I). The second ANOVA, for the average and Hausdorff distance metrics, compared the 3D fast-marching and the manual contours, the manual contours from the two experts (interuser), and the results from the two runs of the algorithm (intersegmentation) (see Table III). Comparisons of the distance metrics were also made between the subgroups to study the performance of the segmentation
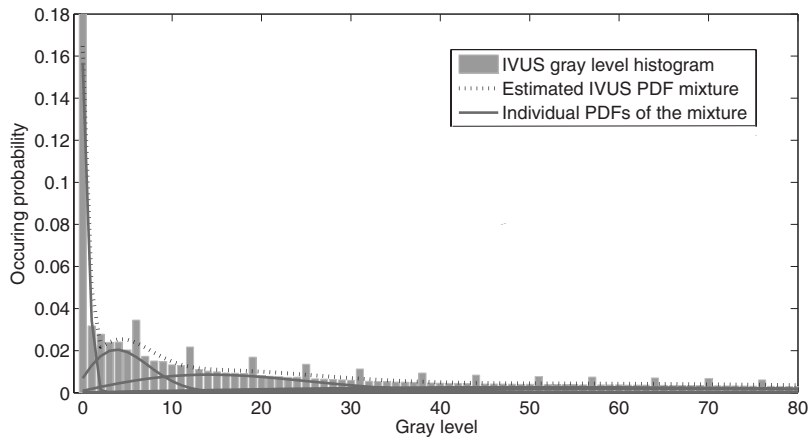
FIG. 5. Detected PDF mixture and corresponding IVUS data histogram. The dotted line corresponds to the global distribution and the solid lines to the individual Rayleigh PDFs. The gray level *x*-axis was shortened for better readability; however, PDFs decreased exponentially for the gray level values up to 256.

on different types of IVUS acquisitions. Finally, the intraclass correlation coefficient was also computed for the area measurements of the manually traced boundaries and segmentation results for the whole database [see Figs. 7(a) and 7(b)]. All statistical analyses were performed with SIGMASTAT, version 3.11, Systat Software Inc., San Jose, CA.

IV. RESULTS

The segmentation method was applied to the 20 IVUS pullbacks of which 7 were acquired before balloon angioplasty, 7 after the intervention and 6 at a 1 year follow-up examination. The lumen and EEM borders were obtained.

IV.A. Preprocessing

IV.A.1. Probability density function estimation

Figure 5 shows an example of automatically detected PDF mixture and corresponding IVUS pullback histogram (a digitization artifact of the IVUS system has probably caused the regularly spaced histogram peaks visible on Fig. 5; however, the PDF mixture estimation process seemed robust to this artifact). The detected mixtures were composed of five Rayleigh distributions even though only four are visible on Fig. 5. In this special case, the fifth PDF is flat with a weight ω_m close to zero because the IVUS pullback PDF mixture could be modeled with less than five distributions.

IV.A.2. Interactive initialization

The fast-marching initialization procedure was performed at the beginning of each segmentation. The interactive acceptance or correction of the EEM longitudinal initial contours was performed on four LViews of each IVUS pullback. The difference between the automatically detected and interactively corrected longitudinal EEM contours was calculated to evaluate the error of the automatically detected boundaries. Average and Hausdorff differences between these contours of 0.14 ± 0.28 and 0.64 ± 0.48 mm were, respectively, found (corresponding to 1.4% and 6.4% of the image dimension).

IV.B. Segmentation

Typical segmentation results for the 3D fast-marching method combining PDFs and gradient are shown in Fig. 6; the manually traced contours by the expert technicians are also displayed. The lumen and EEM boundaries are presented for three different cross-sectional IVUS images. A qualitative analysis of the fast-marching segmentation results reveals detected contours that were very close to all vessel layers.

The area measurements computed from the two runs of the segmentation method and both experts' contours are shown and compared in Table I. The results are reported for the whole IVUS data sets and for each subgroup. For the whole database, statistically significant differences were found between the lumen area measurements from the two experts, and between one of the experts and the segmentation results. For each subgroup, the area measurements from the experts' contours were not statistically significantly different when compared to the segmentation results. No statistically significant difference was found for the EEM area measurements.

Figure 7 shows the correlation between the detected and manually drawn contours for all IVUS sequences. The segmentation results from each run of the algorithm were compared to the manual segmentation of each expert. High intraclass correlation coefficients of 0.966 and 0.989 were, respectively, found for the lumen and EEM areas between the manually traced contours and automated segmentation results. Figure 7 also shows the variation in the area measurements between the detected boundaries and manually drawn contours with the lumen and EEM Bland–Altman plots.

To evaluate the degree of discrepancy between the area measurements, Table II shows the difference (mm^2 and %) between the manually traced and detected boundary areas (Auto-Man column). The results of each run of the segmentation method were compared to each expert. The area differences were evaluated for the preangioplasty, postangioplasty, and follow-up examination data sets. This table also presents the interuser variability (Man-Man column) and the segmentation repeatability (Auto-Auto column).
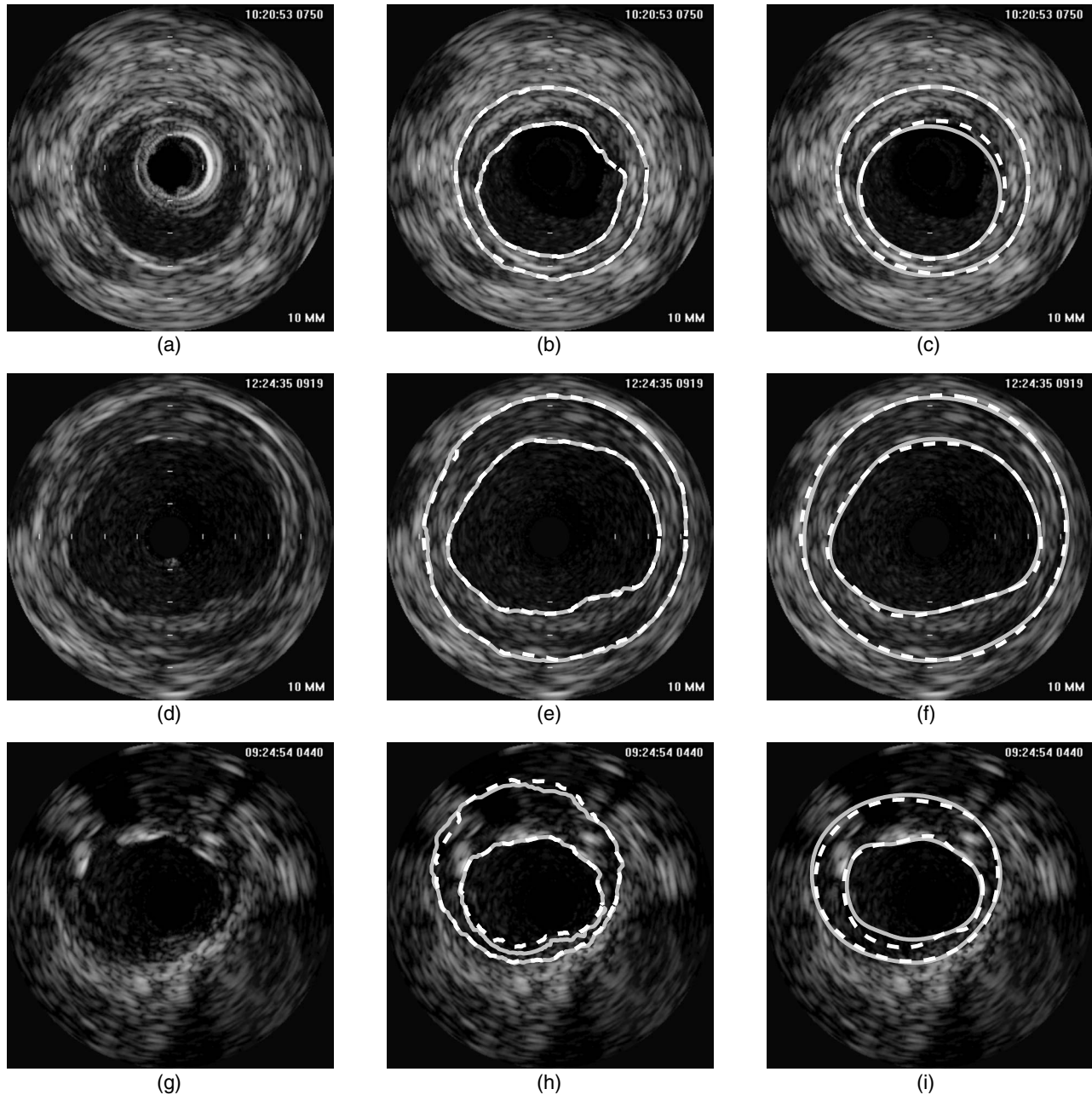
FIG. 6. [(a), (d), (g)] Typical intravascular ultrasound cross-sectional images, [(b), (e), (h)] corresponding segmentation results of the two different runs of the algorithm (solid gray and dashed white sets of contours), [(c), (f), (i)] and manually traced contours by the two experts (solid gray and dashed white sets of contours). Lumen and EEM detected boundaries are depicted. The catheter artifact was removed in (b), (c), (e), (f), (h), and (i). Note that (d) and (g) had almost no catheter artifact. The image size is 10×10 mm^2.

Table III shows the average and Hausdorff distances between the manually traced and detected boundaries (Auto-Man column). The results of each run of the segmentation method were compared to each expert's contours. This table also presents the interuser variability (Man-Man column) and the segmentation repeatability measurements (Auto-Auto column). The average and Hausdorff distances were again computed for the pre-intervention (balloon angioplasty), post-intervention, and follow-up exam acquisitions.

The average and Hausdorff point-to-point contour distances between the automated and manual segmentations were significantly higher than the interuser variability for both contours and for all subgroups (Man-Man column compared to Auto-Man column). However, for the segmentation repeatability, lower average and Hausdorff distances than the interuser variability were obtained for the lumen (Man-Man column compared to Auto-Auto column). For the EEM boundary, the average distance was lower, but the Hausdorff distance was higher when comparing the segmentation variability with that of the expert users.

To investigate the influence of the type of data sets (pre-balloon angioplasty, postballoon angioplasty, and follow-up examination) on the segmentation results, comparisons were also made between the results of the different groups within
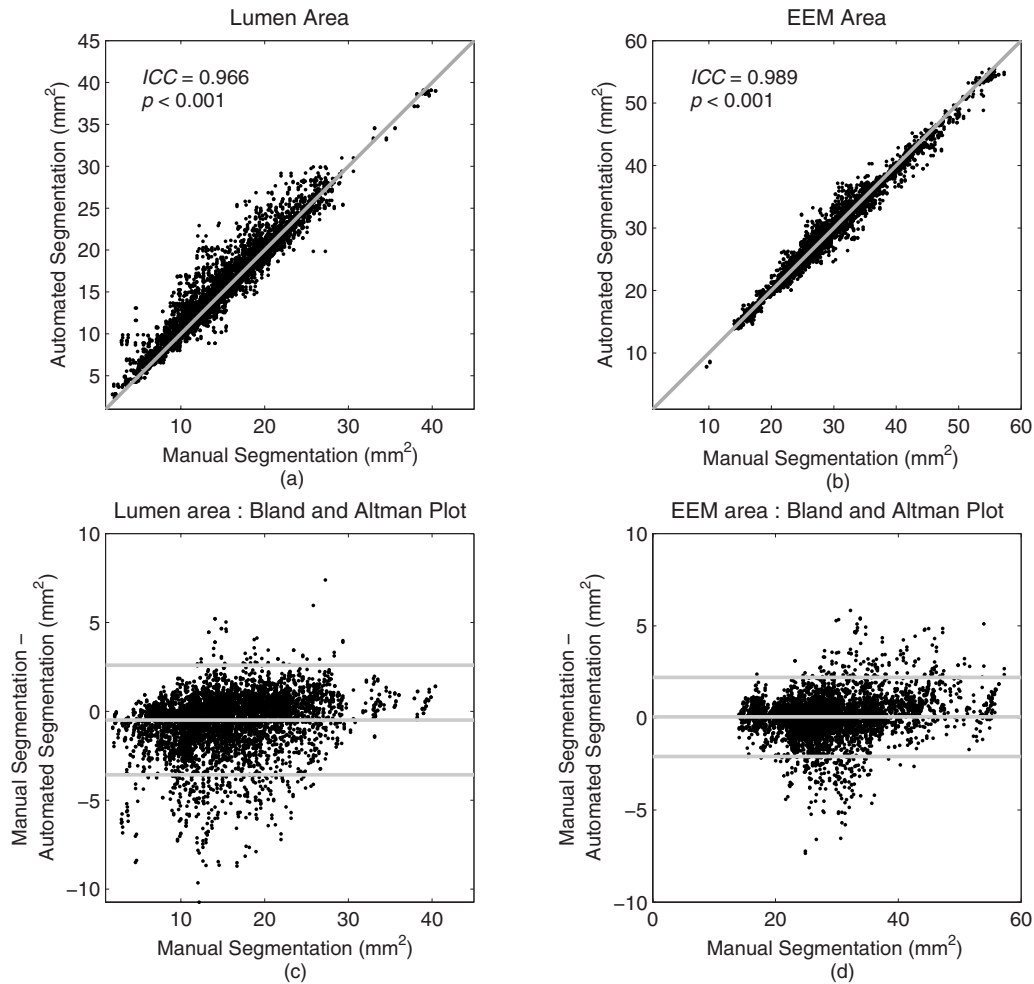
FIG. 7. Area of the detected boundaries versus manually drawn contours for (a) the lumen and (b) the vessel wall for all data sets; the gray lines correspond to $y=x$ and *ICC* is the intraclass correlation coefficient between the detected and manual contour areas. Bland and Altman plots of the area measurements of the detected boundaries and manually drawn contours for (c) the lumen and (d) the vessel wall; the gray lines correspond to the mean ± 2 standard deviations. EEM is the external elastic membrane (the vessel wall border).

each column of Table III. Statistically significant differences were found for many of the error metrics between the different groups. Most often, the post-intervention group produced statistically significant higher error metrics than the pre-intervention and follow-up exam groups.

Figure 8 shows the volumic reconstruction of two IVUS sequences to assess the performance of the method in 3D. The segmented lumen and EEM of the best and worst IVUS pullbacks are displayed. The sequences were rated by an expert radiologist independently of the segmentation results according to their calcium scoring. The worst acquisition contained multiple and severe calcifications. Note that although the manual segmentation technical experts had received the instruction of not segmenting boundaries corrupted by strong calcification shadow, the fast-marching method provided an estimate of those contours.

V. DISCUSSION

A segmentation method based on a combination of global and local image features integrated in a 3D fast-marching model was presented. The segmentation method is highly automated with interactive initialization of the EEM and automatic lumen detection. An extensive validation of the method was performed: A total of 15 895 IVUS frames were segmented and 1524 of these were compared to manually traced contours by IVUS analysis experts. The contributions of this work include the usage of the mixture of the IVUS gray level PDFs and the association of this information to the intensity gradient; a multiple interface fast-marching segmentation using an interactive initialization procedure in which automatically detected EEM contours from only four LViews are accepted or corrected by the user; the processing of femoral artery IVUS images with the segmentation method; and the validation of the segmentation on IVUS acquisitions performed before balloon angioplasty, after the intervention and at a 1 yr follow-up examination.

The preprocessing of the method includes the estimation of a Rayleigh PDF mixture at the beginning of each segmentation; Fig. 5 showed qualitatively that the detected mixture closely fit the corresponding IVUS gray level histogram. Each pullback was thus segmented with its own set of PDF mixture parameters since the acquisition settings were differ-

TABLE II. Segmentation accuracy: Area differences. Man-Man indicates the area difference between the manually traced contours of the two experts, Auto-Man shows the average of the difference between each automated segmentation and each of the expert contours (a positive value indicates a bigger area with the fast-marching method), and Auto-Auto gives the difference between different runs of the 3D fast-marching algorithm. EEM is the external elastic membrane (the vessel wall border). Pre-interv, Post-interv, and Follow-up, respectively, show the results for the pre-intervention (balloon angioplasty), post-intervention, and 1 yr follow-up examination groups. The pixel size is 26×26 μm^2.

	Man-Man	Auto-Man	Auto-Auto
Lumen area difference (mm^2)			
Pre-interv ($N=440$)	-0.71 ± 0.53	0.71 ± 1.70	-0.02 ± 0.45
Post-interv ($N=453$)	-0.94 ± 0.75	0.63 ± 1.38	-0.19 ± 0.96
Follow-up ($N=640$)	-0.67 ± 0.73	0.23 ± 1.16	-0.03 ± 0.46
Lumen area difference (%)			
Pre-interv ($N=440$)	-5.0 ± 5.1	8.3 ± 22.2	-0.2 ± 3.2
Post-interv ($N=453$)	-6.3 ± 5.0	4.4 ± 10.3	-0.8 ± 4.7
Follow-up ($N=640$)	4.9 ± 6.0	3.3 ± 11.1	-0.2 ± 3.1
EEM area difference (mm^2)			
Pre-interv ($N=451$)	-0.07 ± 0.72	0.10 ± 0.94	-0.03 ± 0.52
Post-interv ($N=442$)	-0.03 ± 1.08	-0.07 ± 0.98	0.002 ± 0.97
Follow-up ($N=631$)	-0.24 ± 0.72	-0.15 ± 0.87	0.007 ± 0.59
EEM area difference (%)			
Pre-interv ($N=451$)	-0.3 ± 2.6	0.5 ± 3.7	-0.1 ± 1.9
Post-interv ($N=442$)	-0.1 ± 3.6	-0.2 ± 3.6	0.03 ± 3.1
Follow-up ($N=631$)	-0.8 ± 2.7	-0.4 ± 3.3	0.03 ± 2.3

ent and the echogenicity of the different wall components was variable between patients. A quantitative evaluation was performed earlier and it was shown that the mixture detection was robust and had a low variability.[22] Standard deviations of the mixture parameters ω_m and a_m^2 going from 0.2% to 3.5% were found for several runs of the algorithm on different pixel subsets of an IVUS pullback. The number of distribution in the mixture (five PDFs) was chosen empirically to be high enough to model the different tissue distributions without being too elevated for convergence and computation efficiency. Moreover, with the PDF classification procedure described in Sec. II C 1, a complex plaque could be modeled with more than one Rayleigh distribution. Figure 5 showed that the whole IVUS gray level distribution could be modeled with less than five distributions without altering the segmentation process.

The computation of the fast-marching initial contours was also part of the segmentation preprocessing. The Hausdorff distance between the proposed EEM longitudinal contours on four LViews that were automatically detected and the corrected boundaries was 0.64 mm on average showing that only small corrections were necessary. Moreover, the computation and manual correction of the initial longitudinal EEM contours were completed in 243 ± 161 s per pullback with a combined C and MATLAB implementation of the procedure on an AMD Athlon 64 2 GHz processor with 1 GB of RAM running under Windows XP.

TABLE III. Segmentation accuracy: Average and Hausdorff distances. AD is the average distance (unsigned) and HD is the Hausdorff distance. Man-Man corresponds to the difference metrics between the manually traced contours of the two experts, Auto-Man shows the average of the difference between each automated segmentation and each of the expert contours, and Auto-Auto gives the difference between different runs of the 3D fast-marching algorithm. EEM is the external elastic membrane (the vessel wall border). Pre-interv, Post-interv, and Follow-up, respectively, show the results for the pre-intervention (balloon angioplasty), post-intervention, and 1 yr follow-up examination groups. The pixel size is 26×26 μm^2. No significant difference existed between the subgroups when not indicated. The differences between the columns are not indicated to lighten the table appearance (results from the Auto-Man column were significantly higher than the ones from the Man-Man column).

	Man-Man	Auto-Man	Auto-Auto
Lumen AD (mm)			
Pre-interv ($N=440$)	0.08 ± 0.03 [a]	0.13 ± 0.10 [b]	0.02 ± 0.03 [a]
Post-interv ($N=453$)	0.09 ± 0.04 [a,c]	0.13 ± 0.07 [c]	0.03 ± 0.05 [a,c]
Follow-up ($N=640$)	0.08 ± 0.04 [c]	0.12 ± 0.06 [b,c]	0.02 ± 0.03 [c]
EEM AD (mm)			
Pre-interv ($N=451$)	0.06 ± 0.03 [a]	0.08 ± 0.04	0.03 ± 0.03 [a]
Post-interv ($N=442$)	0.07 ± 0.04 [a,c]	0.09 ± 0.05 [c]	0.05 ± 0.05 [a,c]
Follow-up ($N=631$)	0.06 ± 0.03 [c]	0.08 ± 0.04 [c]	0.03 ± 0.03 [c]
Lumen HD (mm)			
Pre-interv ($N=440$)	0.20 ± 0.10 [a]	0.43 ± 0.30	0.16 ± 0.15 [a]
Post-interv ($N=453$)	0.25 ± 0.13 [a]	0.46 ± 0.26 [c]	0.20 ± 0.21 [a,c]
Follow-up ($N=640$)	0.22 ± 0.12	0.40 ± 0.21 [c]	0.16 ± 0.13 [c]
EEM HD (mm)			
Pre-interv ($N=451$)	0.16 ± 0.09	0.27 ± 0.17	0.17 ± 0.15 [a]
Post-inter ($N=442$)	0.18 ± 0.11 [c]	0.30 ± 0.15 [c]	0.25 ± 0.19 [a,c]
Follow-up ($N=631$)	0.15 ± 0.08 [c]	0.25 ± 0.14 [c]	0.20 ± 0.16 [c]

[a]Indicates statistically significant differences between the pre- and post-intervention groups ($p < 0.01$).
[b]Between the pre-intervention and follow-up exam groups ($p < 0.01$).
[c]Between the post-intervention and follow-up exam groups ($p < 0.01$).

The typical segmentation results that are displayed on Fig. 6 show that the vessel wall boundaries were detected for IVUS images exhibiting different characteristics. A vessel with a large ring-down artifact and a plaque with a hypoechoic section surrounded by a brighter looking thickened intima [Fig. 6(a)] was accurately segmented when comparing the manually drawn and detected contours [Figs. 6(b) and 6(c), respectively]. A robust segmentation was also provided for the large vessel of Fig. 6(d). A vessel that contained calcifications and a heterogeneously looking plaque was segmented in Fig. 6(h). Figures 6(h) and 6(i) show that the largest disagreement between the two experts and between the segmentation results from different runs of the algorithm occurred in the same regions with less information (the lumen contours at 7 o'clock and the EEM contours at 12 o'clock).

A quantitative evaluation of the segmentation accuracy was performed in Tables I and III. The results were compared to manually traced boundaries on approximately 1500 IVUS frames. Table I shows the area measurements computed from both experts and from the segmentation results.
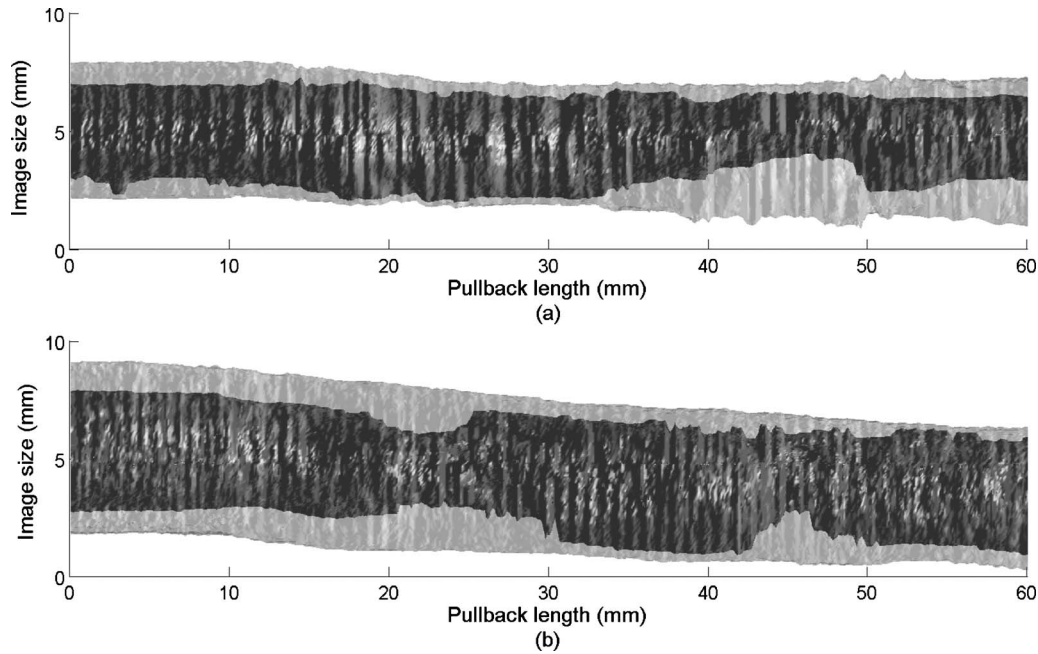
FIG. 8. Volumic reconstructions of the (a) worst and (b) best IVUS pullbacks according to their calcium scoring. The lumen and external elastic membrane boundaries are, respectively, shown in dark and light gray.

Over the whole IVUS database, in Table I, statistically significant differences were found between the two experts' lumen area measurements. This difference shows that the lumen contour was more difficult to identify and led to differences in the IVUS image interpretation. However, these differences were small. The IVUS data were acquired on severely diseased femoral arteries from pre-intervention, post-intervention, and 1 yr follow-up examinations. The average plaque burden, i.e., the area within the EEM occupied by the atherosclerotic plaque,[9] was $47\% \pm 13\%$ with an average maximal value of $71\% \pm 11\%$ (computed from the experts' validation contours). Nonstatistically significant differences of less than 0.2 mm ($p > 0.9$) were obtained between the lumen area measurements from the segmentation contours and one of the experts' manually traced boundaries; a statistically significant difference of 0.9 mm ($p < 0.01$) was found with the other expert's lumen area measurements. However, that difference was small and only slightly higher than the experts' disagreement for the lumen area (0.8 mm). Since the segmentation method was closer to one of the experts' lumen area measurements, that difference was expected. Nonstatistically significant differences of less than 0.1 mm ($p > 0.9$) were measured between the EEM area measurements of the experts and fast-marching segmentation contours.

Table I also showed the area measurements for the preangioplasty, post-intervention, and follow-up examination subgroups. When divided in this manner, no significant difference was found between the segmentation results and the experts' tracings for both contours. This indicates that the lumen and EEM areas can be computed with the fast-marching segmentation in agreement with both experts for the different types of data sets.

Moreover, small area differences between −0.15 and 0.71 mm² were obtained in Table II for the lumen and EEM. These absolute values are in the range of the experts' variability between −0.94 and −0.03 mm² for the lumen and EEM area differences. It is important to evaluate the error on the lumen and EEM area measurements since they are used to evaluate the atherosclerotic disease in terms of stenosis percentage, plaque burden, lumen and vessel wall volumes, and wall thickness.

In addition to these previous results, Fig. 7 showed a high intraclass correlation (>0.96) between the manually traced contours and detected boundaries with the fast-marching method for both lumen and EEM area measurements. The Bland–Altman plots in Figs. 7(c) and 7(d) revealed that the highest errors came from overestimation of the lumen area in some cases. This happened in the presence of a low echogenic plaque or wall making the blood and vessel wall interface hard to identify. An analysis of the ultrasonic speckle that decorrelates in the flowing blood as opposed to the plaque speckle that correlates between adjacent frames might solve this problem and improve the lumen segmentation.

The average and Hausdorff point-to-point distances between contours that were manually traced and detected with the 3D fast-marching segmentation were also reported for the pre-intervention (balloon angioplasty), post-intervention, and follow-up exam acquisitions in Table III. The interobserver and segmentation variabilities were also evaluated. Table III revealed that the point-to-point contour distances between the segmentation results and manual boundaries were significantly higher than the manually traced contour differences (comparison between the columns of Table III). Still, for any type of acquisition, the average and Hausdorff distances of

the segmentation results remained low with values, respectively, under 0.13 and 0.46 mm for both lumen and EEM structures indicating a good performance in general and in regions lacking information or containing artifacts. Again, as shown in Table II, the average and maximum distances corresponded to variations close to the boundaries since small area differences were obtained.

The average and maximum distance results also revealed that the computerized segmentation variability was significantly smaller than the manual interobserver variability according to the point-to-point contour distances except for the EEM Hausdorff distance, but these differences were smaller than 3 pixels (0.07 mm) for all subgroups. The high repeatability of the results shows the low sensitivity of the segmentation method to the EM initialization and to the interactive initialization of the external wall boundary.

When comparing average and Hausdorff distances between the different subgroups (comparison within the columns of Table III), the post-intervention data sets were often more difficult to analyze either manually or computationally as we measured the highest average and Hausdorff distances. However, the discrepancy was small with less than the size of a pixel (0.02 mm) for the average distances and less than 3 pixels (0.08 mm) for the Hausdorff distances. A statistically significant difference was found between the average distance of the pre-intervention and follow-up groups; however, it was less than the size of a pixel (0.01 mm).

Furthermore, Fig. 8 showed qualitatively that the performance of the segmentation method over a whole acquisition was similar for the best and worse IVUS pullbacks. In the presence of severe calcifications, there is no signal or no gray level information behind the calcification arc. In this case, the velocity of the two fronts propagating in opposite directions to detect the EEM boundary was approximately the same; therefore, the fronts converged to the initial boundary for this specific region of the contour only.

To conclude, the multiple interface fast-marching has thus provided segmentation results that were close to the manually traced boundaries by two experts with much less manual interactions. Tables I and III have also shown that the lumen and EEM areas correspond to the experts' analyses, and that the processing of data sets acquired at different time points in a clinical trial (i.e., pre-intervention, post-intervention, and follow-up exams) is feasible with the fast-marching segmentation method.

V.A. Comparison with other segmentation methods

Recently, Giannoglou *et al.*[15] proposed a gradient-based active contour method and found lumen and EEM area differences between segmented and manually traced contours of 0.70 ± 1.34 and 0.17 ± 2.29 mm^2, respectively. Moreover, Bovenkamp *et al.*[17] obtained area differences of -0.14 ± 1.01 and 0.13 ± 2.16 mm^2 for the lumen and EEM, respectively, with an edge-based multiagent segmentation that took up to a minute of processing per image. Takagi *et al.*[10] found lumen and EEM area differences of -0.15 ± 0.84 and -0.18 ± 1.36 mm^2, respectively, with an edge-based graph-search method. These methods are fully automatic and authors obtained area differences roughly in the same range than those obtained with our method but on smaller vessels (coronaries). However, an objective comparison cannot be made without the percentage of area differences that enables comparison regardless of the vessel size. Moreover, in two of these studies, the validation was performed on limited size data sets (less than 200 images[10] and 50 images[15]). Here, we validated our method with 1593 IVUS images that were segmented two times with the computerized algorithm and manually delineated by two experts. In addition, the 3D data sets segmented with the fast-marching method included 15 895 frames.

Sanz-Requena *et al.*[14] also proposed an active contour segmentation method and obtained, for the lumen and EEM, respectively, percentage of area differences of 11.09% and 4.98% for the interactive version of their segmentation and of 10.95% and 7.27% for an automatic segmentation. These values are higher than our 3D fast-marching combining region and local image information that provided differences lower than 8.3% and 0.5% for the lumen and EEM areas, respectively. Koning *et al.*[11] proposed a graph-search-based segmentation method with manual corrections of results if necessary; lumen and EEM area differences of, respectively, -0.21 ± 0.34 and 0.27 ± 0.49 mm^2 were obtained on a small data set (less than 130 images). These values are again in the range of area measurements of our study but on smaller vessels. However, the authors did not provide information on the necessary manual corrections. In our previous work,[22] area differences of 0.40 ± 2.1 and -0.2 ± 2.1 mm^2, average distances of 0.16 ± 0.10 and 0.13 ± 0.07 mm, and Hausdorff distances of 0.40 ± 0.25 and 0.31 ± 0.16 mm, each for the lumen and EEM, respectively, were obtained, which are in the same range of error metrics presented in Tables II and III; these results were obtained with the fast-marching segmentation that was initialized manually. A direct comparison between the previous version of the fast-marching method based only on the gray level PDFs was not performed since the initialization procedure is different. With the new fast-marching method combining the intensity gradient and the gray level PDF mixture, the lumen was fully automatically detected. In addition, minimal interaction, which involved only 4 min on average per IVUS 3D data set for the EEM longitudinal contour calculation and correction, was required for the vessel border initialization.

V.B. Other considerations

The average computation time for the whole segmentation process (PDF mixture, gradient, the initialization computation and interactive correction, and 3D fast-marching) was 1.7 ± 0.3 s per 2D image. The segmentation was not real-time; however, the time to analyze an IVUS data set was dramatically reduced compared to the manual analysis that took approximately 60 s/image, corresponding to a more than 30-fold improvement.

The parameters used in the equations of the initialization procedure (in Sec. II D) were chosen empirically on a subset

of the database to provide neighborhood averaging and flexible deformation windows for all IVUS sequences with small corrections on average. Increasing the size of the windows produced higher computation times without improving the performance of the segmentation. However, some IVUS sequences could have been initialized with less manual corrections if using a different set of parameters specific to the pullback being segmented. Adaptive parameters, optimized for each data set, could decrease the number of necessary manual corrections. It would be conceivable to use the manually corrected contours to compute new parameters for the next frame to be initialized. However, the computation load of such a strategy should remain low to preserve the low computation time.

Moreover, it would be possible to develop a multiscale optimization of the 3D fast-marching segmentation to increase the performance of the method. With this approach, a higher resolution data set is initialized with low resolution segmentation results of the same pullback. At low resolution levels, a larger region can be explored and provides a rough segmentation in less computation time; the segmentation can then be refined at higher resolution levels but with a reduced region to explore. In addition, the initial longitudinal contours could be directly converted to initialize the coarsest data set segmentation; the automatic computation of the initial cross-sectional contours (Sec. II D 2) could thus be eliminated and the computation time decreased.

Another possibility to correct contours that were not initialized with enough precision would be the usage of a generalized fast-marching segmentation method using a speed function that can be either positive or negative.[32] The speed function of Eq. (2) should then be modified to authorize negative values if, for example, the interface propagating toward the lumen boundary was inside the wall instead of being inside the lumen.

A limitation of the method for the processing of IVUS images coming from other types of arteries (such as coronaries) or from other IVUS imaging system might be the usage of Rayleigh distributions in the mixture model. Depending on gain settings, envelop filtering techniques, or other filtering applied to the data by the imaging system, the gray level PDFs of the vessel wall tissues might not be Rayleigh distributed anymore. Other models such as the Nakagami distribution that can still be estimated with the EM algorithm could be used.[33] That would increase the robustness of the segmentation method to the image acquisition parameters and equipment.

Finally, some adjustments of the segmentation method might be required for the processing of coronary IVUS data sets. The size of the windows that defines the neighborhood in the computation of the multiple interface speed functions [Eq. (3)], or the neighborhood of the lumen and EEM boundary likelihood functions [Eq. (8)] would likely need to be adjusted since the size of the coronary wall layers is different. The cardiac motion would also need to be detected during the initialization of the method. Moreover, the assignment of the distributions composing the mixture to the different wall structures for the initial contour calculation

(Sec. II C 1) would also need to be revised to take into account the echogenicity differences between the peripheral and coronary artery vessel wall layers, especially when different scanning frequencies are used.

VI. CONCLUSION

This study has demonstrated the efficiency of the 3D fast-marching segmentation using a combination of Rayleigh PDFs and gray level gradient on *in vivo* intravascular ultrasound images of femoral arteries acquired before and after balloon angioplasty. The segmentation method is highly automated with an interactive initialization procedure. The proposed approach is reliable and has a small variability for the analysis of *in vivo* IVUS images. The usage of the 3D fast-marching segmentation method dramatically reduced the analysis time compared to manual contour tracing. It is hoped that the fast-marching method become a widely used tool for the fastidious and difficult task of IVUS image processing.

ACKNOWLEDGMENTS

a)Electronic mail: marie-helene.roy-cardinal@polymtl.ca

b)Author to whom correspondence should be addressed. Electronic mail: guy.cloutier@umontreal.ca; URL: www.lbum-crchum.com.

[1] A. Guédès, P.-F. Keller, P. L. L'Allier, J. Lespérance, J. Grégoire, and J.-C. Tardif, "Long-term safety of intravascular ultrasound in nontransplant, nonintervened, atherosclerotic coronary arteries," J. Am. Coll. Cardiol. **45**, 559–564 (2005).

[2] J. C. Tardif, J. Grégoire, P. L. L'Allier, R. Ibrahim, J. Lespérance, T. M. Heinonen, S. Kouz, C. Berry, R. Basser, M.-A. Lavoie, M.-C. Guertin, and J. Rodés-Cabau, "Effects of reconstituted high-density lipoprotein infusions on coronary atherosclerosis: A randomized controlled trial," JAMA, J. Am. Med. Assoc. **297**, 1675–1682 (2007).

[3] S. E. Nissen, E. M. Tuzcu, P. Schoenhagen, B. G. Brown, P. Ganz, R. A. Vogel, T. Crowe, G. Howard, C. J. Cooper, B. Brodie, C. L. Grines, and A. N. DeMaria, "Effect of intensive compared with moderate lipid-lowering therapy on progression of coronary atherosclerosis," JAMA, J. Am. Med. Assoc. **291**, 1071–1080 (2004).

[4] D. Böse, C. von Birgelen, and R. Erbel, "Intravascular ultrasound for the evaluation of therapies targeting coronary atherosclerosis," J. Am. Coll. Cardiol. **49**, 925–932 (2007).

[5] J. T. Lee, T. D. Fang, and R. A. White, "Applications of intravascular ultrasound in the treatment of peripheral occlusive disease," Semin Vasc. Surg. **19**, 139–144 (2006).

[6] A. Colombo, P. Hall, S. Nakamura, Y. Almagor, L. Maiello, G. Martini, A. Gaglione, S. L. Goldberg, and J. M. Tobis, "Intracoronary stenting without anticoagulation accomplished with intravascular ultrasound guidance," Circulation **91**, 1676–1688 (1995).

[7] R. Hoffmann, G. S. Mintz, G. R. Dussaillant, J. J. Popma, A. D. Pichard, L. F. Satler, K. M. Ken, J. Griffin, and M. B. Leon, "Patterns and mecha-

nisms of in-stent restenosis: A serial intravascular ultrasound study," Circulation **94**, 1247–1254 (1996).

[8]G. S. Mintz, "Features and parameters of drug-eluting stent deployment discoverable by intravascular ultrasound," Am. J. Cardiol. **100**, 26M–35M (2007).

[9]G. S. Mintz, S. E. Nissen, W. D. Anderson, S. R. Bailey, R. Erbel, P. J. Fitzgerald, F. J. Pinto, K. Rosenfield, R. J. Siegel, E. M. Tuzcu, and P. G. Yock, "American College of Cardiology clinical expert consensus document on standards for acquisition, measurement and reporting of intravascular ultrasound studies (IVUS)," J. Am. Coll. Cardiol. **37**, 1478–1492 (2001).

[10]A. Takagi, K. Hibi, X. Zhang, T. J. Teo, H. N. Bonneau, P. G. Yock, and P. J. Fitzgerald, "Automated contour detection for high-frequency intravascular ultrasound imaging: A technique with blood noise reduction for edge enhancement," Ultrasound Med. Biol. **26**, 1033–1041 (2000).

[11]G. Koning, J. Dijkstra, C. von Birgelen, J. C. Tuinenburg, J. Brunette, J.-C. Tardif, P. W. Oemrawsingh, C. Sieling, S. Melsa, and J. H. C. Reiber, "Advanced contour detection for three-dimensional intracoronary ultrasound: A validation—In vitro and in vivo," Int. J. Card. Imaging **18**, 235–248 (2002).

[12]J. D. Klingensmith, R. Shekhar, and D. G. Vince, "Evaluation of three-dimensional segmentation algorithms for the identification of luminal and medial-adventitial borders in intravascular ultrasound images," IEEE Trans. Med. Imaging **19**, 996–1011 (2000).

[13]G. Kovalski, R. Beyar, R. Shofti, and H. Azhari, "Three-dimensional automatic quantitative analysis of intravascular ultrasound images," Ultrasound Med. Biol. **26**, 527–537 (2000).

[14]R. Sanz-Requena, D. Moratal, D. R. García-Sánchez, V. Bodí, J. J. Rieta, and J. M. Sanchis, "Automatic segmentation and 3D reconstruction of intravascular ultrasound images for a fast preliminar evaluation of vessel pathologies," Comput. Med. Imaging Graph. **31**, 71–80 (2007).

[15]G. D. Giannoglou, Y. S. Chatzizisis, V. Koutkias, I. Kompatsiaris, M. Papadogiorgaki, V. Mezaris, E. Parissi, P. Diamantopoulos, M. G. Strintzis, N. Maglaveras, G. E. Parcharidis, and G. E. Louridas, "A novel active contour model for fully automated segmentation of intravascular ultrasound images: In vivo validation in human coronary arteries," Comput. Biol. Med. **37**, 1292–1302 (2007).

[16]F. Weichert, H. Müller, U. Quast, A. Kraushaar, P. Spilles, M. Heintz, C. Wilke, C. von Birgelen, R. Erbel, and D. Wegener, "Virtual 3D IVUS model for intravascular brachytherapy planning. 3D segmentation, reconstruction, and visualization of coronary artery architecture and orientation," Med. Phys. **30**, 2530–2536 (2003).

[17]E. G. P. Bovenkamp, J. Dijkstra, J. G. Bosch, and J. H. C. Reiber, "Multi-agent segmentation of IVUS images," Pattern Recogn. **37**, 647–663 (2004).

[18]C. Haas, H. Ermert, S. Holt, P. Grewe, A. Machraoui, and J. Barmeyer, "Segmentation of 3D intravascular ultrasonic images based on a random field model," Ultrasound Med. Biol. **26**, 297–306 (2000).

[19]E. Brusseau, C. L. de Korte, F. Mastik, J. Schaar, and A. F. W. van der Steen, "Fully automatic luminal contour segmentation in intracoronary ultrasound imaging—A statistical approach," IEEE Trans. Med. Imaging **23**, 554–566 (2004).

[20]A. Wahle, J. J. Lopez, M. E. Olszewski, S. C. Vigmostad, K. B. Chandran, J. D. Rossen, and M. Sonka, "Plaque development, vessel curvature, and wall shear stress in coronary arteries assessed by x-ray angiography and intravascular ultrasound," Med. Image Anal. **10**, 615–631 (2006).

[21]A. Barker-Hines, in *Peripheral Vascular Diseases*, 5th ed., edited by J. L. Juergens, J. A. Spit-Tell, and J. F. Fairbairn (Saunders, Philadelphia, 1980).

[22]M.-H. Roy Cardinal, J. Meunier, G. Soulez, R. L. Maurice, É. Therasse, and G. Cloutier, "Intravascular ultrasound image segmentation: A three-dimensional fast-marching method based on gray level distributions," IEEE Trans. Med. Imaging **25**, 590–601 (2006).

[23]J. A. Sethian, *Level Set Methods and Fast Marching Methods. Evolving Interfaces in Computational Geometry, Fluids Mechanics, Computer Vision and Materials Science*, 2nd ed. (Cambridge University Press, Cambridge, 1999).

[24]J. A. Sethian, "A fast marching level set method for monotonically advancing fronts," Proc. Natl. Acad. Sci. U.S.A. **93**, 1591–1595 (1996).

[25]R. Malladi, J. A. Sethian, and B. C. Vemuri, "Shape modeling with front propagation: A level set approach," IEEE Trans. Pattern Anal. Mach. Intell. **17**, 158–175 (1995).

[26]E. Sifakis, C. Garcia, and G. Tziritas, "Bayesian level sets for image segmentation," J. Visual Commun. Image Represent **13**, 44–64 (2002).

[27]R. F. Wagner, S. W. Smith, J. M. Sandrik, and H. Lopez, "Statistics of speckle in ultrasound B-scans," IEEE Trans. Sonics Ultrason. **30**, 156–163 (1983).

[28]A. P. Dempster, N. M. Laird, and D. B. Rubin, "Maximum likelihood from incomplete data via the EM algorithm," J. R. Stat. Soc. Ser. B (Methodol.) **39**, 1–38 (1977).

[29]A. K. Jain, Y. Zhong, and S. Lakshmanan, "Object matching using deformable templates," IEEE Trans. Pattern Anal. Mach. Intell. **18**, 267–278 (1996).

[30]E. Therasse, D. Donath, J. Lespérance, J.-C. Tardif, M.-C. Guertin, V. L. Oliva, and G. Soulez, "External beam radiation to prevent restenosis after superficial femoral artery balloon angioplasty," Circulation **111**, 3310–3315 (2005).

[31]V. Chalana and Y. Kim, "A methodology for evaluation of boundary detection algorithms on medical images," IEEE Trans. Med. Imaging **16**, 642–652 (1997).

[32]N. Forcadel, C. Le Guyader, and C. Gout, "Generalized fast marching method: Applications to image segmentation," Numer. Algorithms **48**, 189–211 (2008).

[33]F. Destrempes, J. Meunier, M.-F. Giroux, G. Soulez, and G. Cloutier, "Segmentation in ultrasonic b-mode images of healthy carotid arteries using mixtures of Nakagami distributions and stochastic optimization," IEEE Trans. Med. Imaging **28**, 215–229 (2009).